



Swansea University
Prifysgol Abertawe



Cronfa - Swansea University Open Access Repository

This is an author produced version of a paper published in:
Computer Methods in Applied Mechanics and Engineering

Cronfa URL for this paper:

<http://cronfa.swan.ac.uk/Record/cronfa52110>

Paper:

Vieira, L., Giacomini, M., Sevilla, R. & Huerta, A. (2020). A second-order face-centred finite volume method for elliptic problems. *Computer Methods in Applied Mechanics and Engineering*, 358, 112655
<http://dx.doi.org/10.1016/j.cma.2019.112655>

This item is brought to you by Swansea University. Any person downloading material is agreeing to abide by the terms of the repository licence. Copies of full text items may be used or reproduced in any format or medium, without prior permission for personal research or study, educational or non-commercial purposes only. The copyright for any work remains with the original author unless otherwise specified. The full-text must not be sold in any format or medium without the formal permission of the copyright holder.

Permission for multiple reproductions should be obtained from the original author.

Authors are personally responsible for adhering to copyright and publisher restrictions when uploading content to the repository.

<http://www.swansea.ac.uk/library/researchsupport/ris-support/>

A second-order face-centred finite volume method for elliptic problems

Luan M Vieira^{a,b}, Matteo Giacomini^b, Ruben Sevilla^{a,*}, Antonio Huerta^b

^a*Zienkiewicz Centre for Computational Engineering, College of Engineering, Swansea University, Bay Campus, SA1 8EN, Wales, United Kingdom.*

^b*Laboratori de Calcul Numeric (LaCàN), ETS de Ingenieros de Caminos, Canales y Puertos, Universitat Politècnica de Catalunya Barcelona, Spain.*

Abstract

A second-order face-centred finite volume method (FCFV) is proposed. Contrary to the more popular cell-centred and vertex-centred finite volume (FV) techniques, the proposed method defines the solution on the faces of the mesh (edges in two dimensions). The method is based on a mixed formulation and therefore considers the solution and its gradient as independent unknowns. They are computed solving an element-by-element problem after the solution at the faces is determined. The proposed approach avoids the need of reconstructing the solution gradient, as required by cell-centred and vertex-centred FV methods. This strategy leads to a method that is insensitive to mesh distortion and stretching. The current method is second-order and requires the solution of a global system of equations of identical size and identical number of non-zero elements when compared to the recently proposed first-order FCFV. The formulation is presented for Poisson and Stokes problems. Numerical examples are used to illustrate the approximation properties of the method as well as to demonstrate its potential in three dimensional problems with complex geometries. The integration of a mesh adaptive procedure in

*Corresponding author

Email address: `r.sevilla@swansea.ac.uk` (Ruben Sevilla)

the FCFV solution algorithm is also presented.

Keywords: finite volume method, face-centred, second-order convergence, hybridisable discontinuous Galerkin

1. Introduction

Cell-centred and vertex-centred second-order finite volume (FV) methods are still the predominant techniques used in commercial and industrial computational fluid dynamics (CFD) solvers due to their robustness, easy implementation and relatively low cost [2, 14, 15, 17, 19, 33]. Both, cell-centred and vertex-centred, FV techniques require a reconstruction of the gradient of the solution to ensure second-order convergence of the unknown and first-order convergence of the fluxes [1, 3, 11, 12]. The accuracy of the scheme is therefore dependent on the accuracy of the reconstruction technique, which in turns depends on the quality of the mesh. In particular, FV methods are known to suffer an important loss of accuracy, and sometimes even a loss of second-order convergence, when unstructured meshes are used with highly stretched and/or deformed cells [11, 12].

In [28], the authors proposed a novel methodology called face-centred finite volume (FCFV) method. The technique has many attractive properties when compared to other FV methods. However, the method only provides first-order convergence for the solution.

This paper proposes a second-order FCFV with a computational cost almost identical to the original, first-order, FCFV. The proposed method is still a finite volume approach with constant unknowns on the faces (thus the number of unknowns for the solve have not changed) but features two important differences with respect to the original FCFV. First, the second-order method uses a linear approximation for the primal variable and constant

approximation for the mixed and hybrid variables, rather than a constant approximation for all the variables, as done in the first-order FCFV. Second, the definition of the numerical flux introduces a projection of the primal variable onto the space of constant functions.

Similar to the original FCFV method, the technique proposed here is also insensitive to mesh distortion and stretching and provides a first-order approximation of the gradient of the solution without the need of a reconstruction. The proposed method can also be seen as a particular case of the HDG method by Cockburn and co-workers [5–8] and the HDG methods by [24–26]. Therefore, it inherits the convergence properties of HDG and it passes the LBB condition in the context of incompressible flows.

It is worth mentioning that to obtain second-order accuracy of the primal variable using a standard HDG method with equal order of approximation, polynomial functions of degree one are required to discretise all the variables, including the hybrid one. Hence, the number of globally-coupled degrees of freedom, i.e. the unknowns of the hybrid variable, increases and the size of the global system of equations is substantially larger than in the proposed method. More precisely, in two dimensions the standard HDG method requires the solution of a system twice as large, whereas in three dimensions the system is three times larger.

The proposed second-order FCFV requires the solution of a global system of equations with identical size and number of non-zero elements as the first-order FCFV method. Due to the extra accuracy of the second-order method, compared to the original FCFV [28, 29], this work also proposes a combination of first and second-order methods to produce an error indicator that is used to drive an h -adaptivity process.

Following [12], this paper focuses on elliptic problems to assess the po-

tential of the proposed scheme in the discretisation of viscous fluxes when solving the full Navier-Stokes equations. For this reason, the numerical studies include an analysis of the performance of the scheme in highly stretched meshes, which are responsible for a loss of accuracy in classical FV methods [11, 12] but do not affect the FCFV approach.

The remaining of the paper is organised as follows. In section 2 the proposed second-order FCFV method is presented for the solution of the Poisson equation. Its extension to the Stokes problem is presented in section 3. The ability to combine first-order and second-order FCFV methods to perform an automatic mesh adaptive process is discussed in section 4. Section 5 presents a number of numerical experiments to validate the optimal approximation properties of the method and to compare the accuracy of the first-order and second-order FCFV methods in terms of the computational cost. The insensitivity to mesh distortion and stretching is also demonstrated using numerical experiments. Section 6 presents more challenging problems to show the potential of the proposed second-order FCFV method and its application in an automatic mesh adaptive process. Finally, section 7 summarises the conclusions of the work that has been presented.

2. Second-order FCFV for the Poisson equation

2.1. Problem statement

Let us consider an open bounded domain $\Omega \in \mathbb{R}^{\mathbf{n}_{\text{sd}}}$ with boundary $\partial\Omega = \Gamma_D \cup \Gamma_N$, $\Gamma_D \cap \Gamma_N = \emptyset$ and \mathbf{n}_{sd} the number of spatial dimensions. The strong form of the Poisson problem is

$$\begin{cases} -\nabla \cdot \nabla u = s & \text{in } \Omega, \\ u = u_D & \text{on } \Gamma_D, \\ \mathbf{n} \cdot \nabla u = t & \text{on } \Gamma_N, \end{cases} \quad (1)$$

where s denotes a source term, \mathbf{n} is the outward unit normal vector to the boundary $\partial\Omega$ and u_D and t are the Dirichlet and Neumann data.

The domain Ω is assumed to be partitioned in $\mathbf{n}_{\mathbf{e}1}$ disjoint triangular or tetrahedral cells Ω_e in two and three dimensions respectively

$$\Omega = \bigcup_{e=1}^{\mathbf{n}_{\mathbf{e}1}} \Omega_e, \quad \Omega_e \cap \Omega_l = \emptyset \text{ for } e \neq l, \quad (2)$$

with boundaries $\partial\Omega_e$, defining an internal interface

$$\Gamma := \left[\bigcup_{e=1}^{\mathbf{n}_{\mathbf{e}1}} \partial\Omega_e \right] \setminus \partial\Omega \quad (3)$$

The boundary of a cell is also expressed as the union of a set of edges or faces in two and three dimensions respectively, namely

$$\partial\Omega_e := \bigcup_{j=1}^{\mathbf{n}_{\mathbf{f}a}^e} \Gamma_{e,j}, \quad (4)$$

where $\mathbf{n}_{\mathbf{f}a}^e$ denotes the number of edges/faces of the cell Ω_e . For triangular cells $\mathbf{n}_{\mathbf{f}a}^e = 3$ and for tetrahedral cells $\mathbf{n}_{\mathbf{f}a}^e = 4$.

The proposed FCFV method uses the mixed form of the Poisson problem in the so-called *broken* computational domain, namely

$$\left\{ \begin{array}{l} \mathbf{q} + \nabla u = \mathbf{0} \quad \text{in } \Omega_e, \text{ and for } e = 1, \dots, \mathbf{n}_{\mathbf{e}1}, \\ \nabla \cdot \mathbf{q} = s \quad \text{in } \Omega_e, \text{ and for } e = 1, \dots, \mathbf{n}_{\mathbf{e}1}, \\ u = u_D \quad \text{on } \Gamma_D, \\ \mathbf{n} \cdot \mathbf{q} = -t \quad \text{on } \Gamma_N, \\ \llbracket u \mathbf{n} \rrbracket = \mathbf{0} \quad \text{on } \Gamma, \\ \llbracket \mathbf{n} \cdot \mathbf{q} \rrbracket = 0 \quad \text{on } \Gamma, \end{array} \right. \quad (5)$$

where, following [18], the jump operator is defined as the sum of the values from the left and right of an interface, that is $\llbracket \odot \rrbracket = \odot_e + \odot_l$.

It is worth noting that the last two equations in (5) impose the continuity of the solution and the normal flux across the interface Γ , respectively.

2.2. Strong form of the local and global problems

As it is usual in HDG methods [8, 20, 21, 31] and FCFV methods, the strong form of the problem is split into the so-called local problem, defined element-by-element,

$$\left\{ \begin{array}{ll} \mathbf{q}_e + \nabla u_e = \mathbf{0} & \text{in } \Omega_e, \\ \nabla \cdot \mathbf{q}_e = s & \text{in } \Omega_e, \\ u_e = u_D & \text{on } \partial\Omega_e \cap \Gamma_D, \\ u_e = \hat{u} & \text{on } \partial\Omega_e \setminus \Gamma_D, \end{array} \right. \quad (6)$$

for $e = 1, \dots, \mathbf{n}_{e1}$, and the global problem, defined over the interface Γ and the Neumann boundary

$$\left\{ \begin{array}{ll} \llbracket u\mathbf{n} \rrbracket = \mathbf{0} & \text{on } \Gamma, \\ \llbracket \mathbf{n} \cdot \mathbf{q} \rrbracket = 0 & \text{on } \Gamma, \\ \mathbf{n} \cdot \mathbf{q} = -t & \text{on } \Gamma_N. \end{array} \right. \quad (7)$$

The local problem (6) is a pure Dirichlet problem defined on each cell and introduces the value of the solution at the cell faces, \hat{u} , as an independent variable.

Remark 1. *The first equation in (7) is automatically satisfied due to the imposition of the Dirichlet boundary condition in the local problem and the unique value of \hat{u} on the interior faces*

2.3. Second-order FCFV weak formulation

Let us denote by $\mathcal{V}^1(\Omega)$ the space of $\mathcal{L}_2(\Omega)$ functions that are, at most, linear in each cell, $\mathcal{V}^0(\Omega)$ the space of $\mathcal{L}_2(\Omega)$ functions that are constant in each cell and $\hat{\mathcal{V}}^0(\Gamma)$ the space of $\mathcal{L}_2(\Gamma)$ functions that are constant on each

cell face. With these definitions, the discrete weak formulation of the local problem is: find $(u_e^h, \mathbf{q}_e^h) \in \mathcal{V}^1(\Omega_e) \times [\mathcal{V}^0(\Omega_e)]^{\mathbf{n}_{\text{sd}}}$ such that

$$-\int_{\Omega_e} \mathbf{q}_e^h d\Omega = \int_{\partial\Omega_e \cap \Gamma_D} u_D \mathbf{n}_e d\Gamma + \int_{\partial\Omega_e \setminus \Gamma_D} \hat{u}^h \mathbf{n}_e d\Gamma, \quad (8)$$

$$-\int_{\Omega_e} \nabla v \cdot \mathbf{q}_e^h d\Omega + \int_{\partial\Omega_e} v (\mathbf{n}_e \cdot \hat{\mathbf{q}}_e^h) d\Gamma = \int_{\Omega_e} v s d\Omega \quad (9)$$

for all $v \in \mathcal{V}^1(\Omega_e)$ and for $e = 1, \dots, \mathbf{n}_{e1}$. It is worth noting that in equation (8), a constant test function has been arbitrarily chosen in the space $[\mathcal{V}^0(\Omega_e)]^{\mathbf{n}_{\text{sd}}}$ and it has been used that $\mathbf{q}_e^h \in [\mathcal{V}^0(\Omega_e)]^{\mathbf{n}_{\text{sd}}}$, that is $\nabla \cdot \mathbf{q}_e^h = 0$.

The so-called numerical flux, $\hat{\mathbf{q}}_e^h$, is defined as

$$\mathbf{n}_e \cdot \hat{\mathbf{q}}_e^h := \begin{cases} \mathbf{n}_e \cdot \mathbf{q}_e^h + \tau_e (\mathbb{P}_0 u_e^h - u_D) & \text{on } \partial\Omega_e \cap \Gamma_D, \\ \mathbf{n}_e \cdot \mathbf{q}_e^h + \tau_e (\mathbb{P}_0 u_e^h - \hat{u}^h) & \text{elsewhere,} \end{cases} \quad (10)$$

where \mathbb{P}_0 denotes the projection operator over the space of constant functions [24, 25] and τ_e is a stabilisation parameter. The parameter τ_e is selected to ensure stability and accuracy of the resulting scheme. The importance of the stabilisation parameter has been extensively studied in the work by Cockburn and co-workers [4, 8, 20–23].

Remark 2. *There are two differences between the scheme proposed here and the original FCFV [28]. First, here the primal variable is approximated using piecewise linear polynomials, whereas in the first-order FCFV method piecewise constant functions are used. Second, the definition of the numerical flux considered here follows the rationale of the hybridised DG method with reduced stabilisation [24], by introducing the projection operator \mathbb{P}_0 . As discussed in [24], if the projection operator is not introduced in equation (10), the resulting method is only first-order accurate, providing no advantages with respect to the original FCFV. Therefore, the use of the projection operator,*

together with a richer space for approximating the primal variable, is required to obtain a second-order accurate scheme.

Introducing the expression of the numerical flux in equation (9) and integrating by parts the first term, leads to the following discrete weak formulation: find $(u_e^h, \mathbf{q}_e^h) \in \mathcal{V}^1(\Omega_e) \times [\mathcal{V}^0(\Omega_e)]^{\mathbf{n}_{\text{sd}}}$ such that

$$-\int_{\Omega_e} \mathbf{q}_e^h d\Omega = \int_{\partial\Omega_e \cap \Gamma_D} u_D \mathbf{n}_e d\Gamma + \int_{\partial\Omega_e \setminus \Gamma_D} \hat{u}^h \mathbf{n}_e d\Gamma, \quad (11)$$

$$\int_{\partial\Omega_e} v \tau_e \mathbb{P}_0 u_e^h d\Gamma = \int_{\Omega_e} v s d\Omega + \int_{\partial\Omega_e \cap \Gamma_D} v \tau_e u_D d\Gamma + \int_{\partial\Omega_e \setminus \Gamma_D} v \tau_e \hat{u}^h d\Gamma \quad (12)$$

for all $v \in \mathcal{V}^1(\Omega_e)$ and for $e = 1, \dots, \mathbf{n}_{e1}$.

The discrete weak form of the global problem is obtained following an analogous process. It becomes: find $\hat{u}^h \in \hat{\mathcal{V}}^0(\Gamma \cup \Gamma_N)$ such that

$$\sum_{e=1}^{\mathbf{n}_{e1}} \int_{\partial\Omega_e \setminus \Gamma_D} \mathbf{n}_e \cdot \hat{\mathbf{q}}_e^h d\Gamma = - \sum_{e=1}^{\mathbf{n}_{e1}} \int_{\partial\Omega_e \cap \Gamma_N} t d\Gamma, \quad (13)$$

a constant test function has been arbitrarily chosen in the space $\hat{\mathcal{V}}^0(\Gamma \cup \Gamma_N)$.

Introducing the definition of the numerical flux in equation (13) leads to the following weak form of the global problem: find $\hat{u}^h \in \hat{\mathcal{V}}^0(\Gamma \cup \Gamma_N)$ such that

$$\sum_{e=1}^{\mathbf{n}_{e1}} \int_{\partial\Omega_e \setminus \Gamma_D} (\mathbf{n}_e \cdot \mathbf{q}_e^h + \tau_e (\mathbb{P}_0 u_e^h - \hat{u}^h)) d\Gamma = - \sum_{e=1}^{\mathbf{n}_{e1}} \int_{\partial\Omega_e \cap \Gamma_N} t d\Gamma. \quad (14)$$

2.4. Second-order FCFV discretisation

To simplify the notation, the following sets of faces are introduced

$$\begin{aligned} \mathcal{A}_e &:= \{1, \dots, \mathbf{n}_{\text{fa}}^e\}, \\ \mathcal{D}_e &:= \{j \in \mathcal{A}_e \mid \Gamma_{e,j} \cap \Gamma_D \neq \emptyset\}, \\ \mathcal{N}_e &:= \{j \in \mathcal{A}_e \mid \Gamma_{e,j} \cap \Gamma_N \neq \emptyset\}, \\ \mathcal{B}_e &:= \mathcal{A}_e \setminus \mathcal{D}_e = \{j \in \mathcal{A}_e \mid \Gamma_{e,j} \cap \Gamma_D = \emptyset\}, \end{aligned} \quad (15)$$

corresponding to all faces of a cell, the faces on the Dirichlet boundary, the faces on the Neumann boundary and the faces not on the Dirichlet boundary, respectively. It is also convenient to denote the set of nodes of a cell Ω_e belonging to a face $\Gamma_{e,j}$ as $\mathcal{F}_{e,j}$. Finally, the indicator function of a set \square is defined as

$$\chi_{\square}(l) = \begin{cases} 1 & \text{if } l \in \square \\ 0 & \text{otherwise.} \end{cases} \quad (16)$$

With this notation, the discrete local problem becomes

$$-|\Omega_e|\mathbf{q}_e = \sum_{j \in \mathcal{D}_e} |\Gamma_{e,j}| \mathbf{n}_j u_{D,j} + \sum_{j \in \mathcal{B}_e} |\Gamma_{e,j}| \mathbf{n}_j \hat{u}_j, \quad (17a)$$

$$\mathbf{m}_e \mathbf{u}_e = \mathbf{f}_e + \sum_{j \in \mathcal{D}_e} \tau_j \mathbf{d}_j + \sum_{j \in \mathcal{B}_e} \tau_j \mathbf{r}_j \hat{u}_j, \quad (17b)$$

where τ_j denotes the value of the stabilisation parameter on the j -th face, assumed constant, \mathbf{q}_e contains the value of \mathbf{q} in the cell and \mathbf{u}_e contains the nodal values of the solution in the cell. The matrices and vectors in equation (17b) are given by

$$(m_e)_{IJ} := \sum_{k=1}^{\mathbf{n}_{\text{fa}}^e} \frac{1}{\mathbf{n}_{\text{fn}}^{e,i}} |\Gamma_{e,k}| \tau_k \chi_{\mathcal{F}_{e,k}}(I) (p_{e,i})_J, \quad (f_e)_I := \frac{1}{\mathbf{n}_{\text{en}}} s_e |\Omega_e|, \quad (18)$$

$$(d_j)_I := \frac{1}{\mathbf{n}_{\text{fn}}^{e,i}} u_{D,j} |\Gamma_{e,j}|, \quad (r_j)_I := \frac{1}{\mathbf{n}_{\text{fn}}^{e,i}} |\Gamma_{e,j}| \delta_{Ij}, \quad (19)$$

where \mathbf{n}_{en} is the number of cell nodes, the vector $\mathbf{p}_{e,i}$ is introduced to compute the projection of the solution, i.e. the average of the nodal values of \mathbf{u}_e on face $\Gamma_{e,i}$. Formally it is defined as

$$(p_{e,i})_l = \frac{1}{\mathbf{n}_{\text{fn}}^{e,i}} \chi_{\mathcal{F}_{e,i}}(l) \quad (20)$$

with $\mathbf{n}_{\text{fn}}^{e,i}$ being the number of nodes of the face $\Gamma_{e,i}$.

The discrete local problem allows to obtain an explicit expression of both the solution and its gradient in terms of the solution at the cell faces/edges,

namely

$$\mathbf{q}_e = -|\Omega_e|^{-1}\mathbf{z}_e - |\Omega_e|^{-1} \sum_{j \in \mathcal{B}_e} |\Gamma_{e,j}| \mathbf{n}_j \hat{u}_j, \quad (21a)$$

$$\mathbf{u}_e = \mathbf{m}_e^{-1} \mathbf{b}_e + \mathbf{m}_e^{-1} \sum_{j \in \mathcal{B}_e} \tau_j \mathbf{r}_j \hat{u}_j, \quad (21b)$$

where

$$\mathbf{b}_e := \mathbf{f}_e + \sum_{j \in \mathcal{D}_e} \tau_j \mathbf{d}_j, \quad \mathbf{z}_e := \sum_{j \in \mathcal{D}_e} |\Gamma_{e,j}| \mathbf{n}_j u_{D,j}. \quad (22)$$

It is worth noting that equation (21b) involves the solution of a 3×3 system of equations for triangular cells and a 4×4 system for tetrahedral cells. Given the size of the system and the definition of \mathbf{m}_e , its inverse can be analytically computed to reduce the computational cost of this operation.

The discretisation of the global problem of equation (14) leads, for $i \in \mathcal{B}_e$, to

$$\sum_{e=1}^{\text{nel}} \left\{ |\Gamma_{e,i}| \mathbf{n}_i \cdot \mathbf{q}_e + |\Gamma_{e,i}| \tau_i \mathbf{p}_{e,i} \cdot \mathbf{u}_e - |\Gamma_{e,i}| \tau_i \hat{u}_i \right\} = - \sum_{e=1}^{\text{nel}} \left\{ |\Gamma_{e,i}| t_i \chi_{\mathcal{N}_e}(i) \right\}. \quad (23)$$

By inserting the explicit expressions of equation (21), in the global problem of equation (23), a linear system of equations involving only the solution on the faces as an unknown is obtained, namely

$$\widehat{\mathbf{K}} \hat{\mathbf{u}} = \hat{\mathbf{f}}. \quad (24)$$

The global matrix $\widehat{\mathbf{K}}$ and right hand side $\hat{\mathbf{f}}$ are obtained by assembling the in the cell contributions given by

$$\widehat{K}_{i,j}^e := |\Gamma_{e,i}| \left(\tau_i \tau_j \mathbf{p}_{e,i} \cdot (\mathbf{m}_e^{-1} \mathbf{r}_j) - |\Omega_e|^{-1} |\Gamma_{e,j}| \mathbf{n}_i \cdot \mathbf{n}_j - \tau_i \delta_{ij} \right), \quad (25a)$$

$$\widehat{f}_i^e := |\Gamma_{e,i}| \left(|\Omega_e|^{-1} \mathbf{n}_i \cdot \mathbf{z}_e - \tau_i \mathbf{p}_{e,i} \cdot (\mathbf{m}_e^{-1} \mathbf{b}_e) - t_i \chi_{\mathcal{N}_e}(i) \right), \quad (25b)$$

for $i, j \in \mathcal{B}_e$ and with δ_{ij} denoting the Kronecker delta.

As discussed in remark 2, the use of the projection operator in the numerical flux of equation (10) is required to obtain a second-order method. If

the projection is not introduced, the resulting method is only first-order [24]. This minor difference is exploited in section 4 to devise an error indicator that can be used to drive an automatic mesh adaptive process. Therefore, it is of interest here to study the difference in the global system of equation (25) induced by the introduction of the projection operator. The next result shows that only the matrix \mathbf{m}_e changes if the projection is not considered.

Lemma 1. *Let us consider a face $\Gamma_{e,i}$ of a triangular or tetrahedral cell Ω_e and $u_e^h \in \mathcal{V}^1(\Omega_e)$. Then, the following equality holds*

$$\int_{\Gamma_{e,i}} \mathbb{P}_0 u_e^h d\Gamma = \int_{\Gamma_{e,i}} u_e^h d\Gamma. \quad (26)$$

Proof. The first integral of equation (26) can be written as

$$\int_{\Gamma_{e,i}} \mathbb{P}_0 u_e^h d\Gamma = |\Gamma_{e,i}| \mathbb{P}_0 u_e^h = |\Gamma_{e,i}| \mathbf{p}_{e,i} \cdot \mathbf{u}_e \quad (27)$$

because $\mathbb{P}_0 u_e^h$ is constant within each face.

The second integral of equation (26) can be easily computed using the expression of the linear shape functions used to define the approximation u_e^h , namely

$$\int_{\Gamma_{e,i}} u_e^h d\Gamma = \sum_{l=1}^{n_{en}} \left(\int_{\Gamma_{e,i}} N_l d\Gamma \right) u_l = \sum_{l=1}^{n_{en}} \left(\frac{1}{n_{fn}^{e,i}} |\Gamma_{e,i}| \chi_{\mathcal{F}_{e,i}}(l) \right) u_l. \quad (28)$$

where N_l and u_l denote the linear shape function and nodal value associated with the l -th node.

Equality (26) follows from the definition of $\mathbf{p}_{e,i}$ introduced in equation (20). □

3. Second-order FCFV for the Stokes equation

3.1. Problem statement

The strong form of the Stokes problem can be written in the partitioned domain and after splitting the second-order momentum conservation equa-

tion into a system of two first-order equations, as

$$\left\{ \begin{array}{ll} \mathbf{L} + \sqrt{\nu} \nabla \mathbf{u} = \mathbf{0} & \text{in } \Omega_e, \text{ and for } e = 1, \dots, \mathbf{n}_{e1}, \\ \nabla \cdot (\sqrt{\nu} \mathbf{L} + p \mathbf{I}_{\mathbf{n}_{sd}}) = \mathbf{s} & \text{in } \Omega_e, \text{ and for } e = 1, \dots, \mathbf{n}_{e1}, \\ \nabla \cdot \mathbf{u} = 0 & \text{in } \Omega_e, \text{ and for } e = 1, \dots, \mathbf{n}_{e1}, \\ \mathbf{u} = \mathbf{u}_D & \text{on } \Gamma_D, \\ \mathbf{n} \cdot (\sqrt{\nu} \mathbf{L} + p \mathbf{I}_{\mathbf{n}_{sd}}) = -\mathbf{t} & \text{on } \Gamma_N, \\ \llbracket \mathbf{u} \otimes \mathbf{n} \rrbracket = \mathbf{0} & \text{on } \Gamma, \\ \llbracket \mathbf{n} \cdot (\sqrt{\nu} \mathbf{L} + p \mathbf{I}_{\mathbf{n}_{sd}}) \rrbracket = \mathbf{0} & \text{on } \Gamma. \end{array} \right. \quad (29)$$

where $\nu > 0$ is the viscosity and the last two equations enforce the continuity of the velocity and the normal flux across the interface Γ respectively.

Remark 3. *To simplify the presentation, this work considers the traditional velocity-pressure HDG formulation of the Stokes equation [32], where the vector \mathbf{t} does not correspond to the boundary traction and it is usually called a pseudo-traction [13]. It is worth emphasising that the so-called Cauchy formulation could also be employed here, using the formulation proposed in [16]. This formulation, contrary to other existing HDG methods, guarantees optimal convergence even for low order approximations. This idea was also exploited in the context of linear elasticity to obtain optimal convergence for low order approximations in an HDG context [27, 29, 30].*

3.2. Strong form of the local and global problems

As usually done in HDG methods [9, 16, 25] and FCFV methods, the strong form of the problem given by equation (29) is split into the local and

global problems. The local problem

$$\left\{ \begin{array}{ll} \mathbf{L}_e + \sqrt{\nu} \nabla \mathbf{u}_e = \mathbf{0} & \text{in } \Omega_e, \\ \nabla \cdot (\sqrt{\nu} \mathbf{L}_e + p_e \mathbf{I}_{\text{nsd}}) = \mathbf{s} & \text{in } \Omega_e, \\ \nabla \cdot \mathbf{u}_e = 0 & \text{in } \Omega_e \\ \mathbf{u}_e = \mathbf{u}_D & \text{on } \partial\Omega_e \cap \Gamma_D, \\ \mathbf{u}_e = \hat{\mathbf{u}} & \text{on } \partial\Omega_e \setminus \Gamma_D. \end{array} \right. \quad (30)$$

is a pure Dirichlet problem and, therefore, requires the introduction of a solvability constraint for the pressure [9], namely

$$\frac{1}{|\partial\Omega_e|} \int_{\partial\Omega_e} p_e d\Gamma = \rho_e \quad (31)$$

where ρ_e is the mean value of the pressure on the boundary of the cell Ω_e .

In addition, a compatibility condition is induced by the free-divergence character of the velocity, namely

$$\int_{\partial\Omega_e \setminus \Gamma_D} \hat{\mathbf{u}} \cdot \mathbf{n}_e d\Gamma + \int_{\partial\Omega_e \cap \Gamma_D} \mathbf{u}_D \cdot \mathbf{n}_e d\Gamma = 0. \quad (32)$$

As the continuity of the solution is automatically imposed by the introduction of the velocity on the cell faces as an independent variable that is uniquely defined on each face, the global problem imposes the continuity of the normal flux across the interface and the Neumann boundary conditions, that is

$$\left\{ \begin{array}{ll} \llbracket \mathbf{n} \cdot (\sqrt{\nu} \mathbf{L} + p \mathbf{I}_{\text{nsd}}) \rrbracket = \mathbf{0} & \text{on } \Gamma, \\ \mathbf{n} \cdot (\sqrt{\nu} \mathbf{L} + p \mathbf{I}_{\text{nsd}}) = -\mathbf{t} & \text{on } \Gamma_N. \end{array} \right. \quad (33)$$

3.3. Second-order FCFV weak formulation

Following the same rationale presented for the Poisson problem, the discrete weak formulation of the local Stokes problem is: find $(\mathbf{u}_e^h, \mathbf{L}_e^h, p_e^h) \in$

$[\mathcal{V}^1(\Omega_e)]^{\text{nsd}} \times [\mathcal{V}^0(\Omega_e)]^{\text{nsd} \times \text{nsd}} \times [\mathcal{V}^0(\Omega_e)]$ such that

$$- \int_{\Omega_e} \mathbf{L}_e^h d\Omega = \int_{\partial\Omega_e \cap \Gamma_D} \sqrt{\nu} \mathbf{n}_e \otimes \mathbf{u}_D d\Gamma + \int_{\partial\Omega_e \setminus \Gamma_D} \sqrt{\nu} \mathbf{n}_e \otimes \widehat{\mathbf{u}}^h d\Gamma, \quad (34a)$$

$$\int_{\partial\Omega_e} \tau_e \mathbf{w} \cdot \mathbb{P}_0 \mathbf{u}_e^h d\Gamma = \int_{\Omega_e} \mathbf{w} \cdot \mathbf{s} d\Omega + \int_{\partial\Omega_e \cap \Gamma_D} \tau_e \mathbf{w} \cdot \mathbf{u}_D d\Gamma + \int_{\partial\Omega_e \setminus \Gamma_D} \tau_e \mathbf{w} \cdot \widehat{\mathbf{u}}^h d\Gamma, \quad (34b)$$

$$\int_{\partial\Omega_e \setminus \Gamma_D} \widehat{\mathbf{u}} \cdot \mathbf{n}_e d\Gamma + \int_{\partial\Omega_e \cap \Gamma_D} \mathbf{u}_D \cdot \mathbf{n}_e d\Gamma = 0, \quad (34c)$$

$$\frac{1}{|\partial\Omega_e|} \int_{\partial\Omega_e} p_e^h d\Gamma = \rho_e, \quad (34d)$$

for all $\mathbf{w} \in [\mathcal{V}^1(\Omega_e)]^{\text{nsd}}$. It is worth emphasising that in equations (34a) and (34c), a constant test function has been arbitrarily chosen in the spaces $[\mathcal{V}^0(\Omega_e)]^{\text{nsd} \times \text{nsd}}$ and $\mathcal{V}^0(\Omega_e)$ respectively. It is also worth noting that equation (34c) is exactly the compatibility condition introduced in equation (32). As done in the standard FCFV method, this equation is then removed from the local problem and imposed only in the global problem.

The weak form of the local problem has been introduced after using the following definition of the numerical flux

$$\mathbf{n}_e \cdot (\widehat{\sqrt{\nu} \mathbf{L}_e^h + p_e^h \mathbf{I}_{\text{nsd}}}) := \begin{cases} \mathbf{n}_e \cdot (\sqrt{\nu} \mathbf{L}_e^h + p_e^h \mathbf{I}_{\text{nsd}}) + \tau_e (\mathbb{P}_0 \mathbf{u}_e^h - \mathbf{u}_D) & \text{on } \partial\Omega_e \cap \Gamma_D, \\ \mathbf{n}_e \cdot (\sqrt{\nu} \mathbf{L}_e^h + p_e^h \mathbf{I}_{\text{nsd}}) + \tau_e (\mathbb{P}_0 \mathbf{u}_e^h - \widehat{\mathbf{u}}^h) & \text{elsewhere.} \end{cases} \quad (35)$$

The discrete global problem that accounts for the transmission conditions, the Neumann boundary condition and the incompressibility constraint reads: find $(\widehat{\mathbf{u}}^h, \rho_e) \in [\widehat{\mathcal{V}}^0(\Gamma \cup \Gamma_N)]^{\text{nsd}} \times \mathbb{R}$ such that

$$\sum_{e=1}^{\mathbf{n}_{e1}} \int_{\partial\Omega_e \setminus \Gamma_D} \left(\sqrt{\nu} \mathbf{n}_e \cdot \mathbf{L}_e^h + p_e^h \mathbf{n}_e + \tau_e (\mathbb{P}_0 \mathbf{u}_e^h - \widehat{\mathbf{u}}^h) \right) d\Gamma = - \sum_{e=1}^{\mathbf{n}_{e1}} \int_{\partial\Omega_e \cap \Gamma_N} \mathbf{t} d\Gamma, \quad (36a)$$

$$\int_{\partial\Omega_e \setminus \Gamma_D} \widehat{\mathbf{u}} \cdot \mathbf{n}_e d\Gamma + \int_{\partial\Omega_e \cap \Gamma_D} \mathbf{u}_D \cdot \mathbf{n}_e d\Gamma = 0 \quad \text{for } e = 1, \dots, \mathbf{n}_{e1}. \quad (36b)$$

It is worth noting that a constant test function in the space $[\hat{\mathcal{V}}^0(\Gamma \cup \Gamma_N)]^{\mathbf{n}_{\text{sd}}}$ has been used in equation (36a).

3.4. Second-order FCFV discretisation

Using the notation introduced in section 2.4, the discrete local Stokes problem provides explicit expressions of the velocity, its gradient and the pressure in terms of the velocity on the faces and the mean pressure. The expressions are

$$\mathbf{L}_e = -|\Omega_e|^{-1}\sqrt{\nu}\mathbf{Z}_e - |\Omega_e|^{-1}\sqrt{\nu}\sum_{j \in \mathcal{B}_e} |\Gamma_{e,j}| \mathbf{n}_j \otimes \hat{\mathbf{u}}_j, \quad (37a)$$

$$\mathbf{u}_e = \mathbf{M}_e^{-1}\mathbf{B}_e + \mathbf{M}_e^{-1}\sum_{j \in \mathcal{B}_e} \tau_j \mathbf{R}_j \hat{\mathbf{u}}_j, \quad (37b)$$

$$p_e = \rho_e, \quad (37c)$$

for $e = 1, \dots, \mathbf{n}_{\text{el}}$, where

$$\mathbf{B}_e := \mathbf{F}_e + \sum_{j \in \mathcal{D}_e} \tau_j \mathbf{D}_j, \quad \mathbf{Z}_e := \sum_{j \in \mathcal{D}_e} |\Gamma_{e,j}| \mathbf{n}_j \otimes \mathbf{u}_{D,j}. \quad (38)$$

and

$$\begin{aligned} (\mathbf{M}_e)_{IJ} &:= \mathbf{I}_{\mathbf{n}_{\text{sd}}} \sum_{k=1}^{\mathbf{n}_{\text{fa}}^e} \frac{1}{\mathbf{n}_{\text{fn}}^{e,i}} |\Gamma_{e,k}| \tau_k \chi_{\mathcal{F}_{e,k}}(I) (p_{e,i})_J, & \mathbf{F}_I &:= \frac{1}{\mathbf{n}_{\text{en}}} \mathbf{s}_e |\Omega_e|, \\ (\mathbf{D}_j)_I &:= \frac{1}{\mathbf{n}_{\text{fn}}^{e,i}} \mathbf{u}_{D,j} |\Gamma_{e,j}|, & (\mathbf{R}_j)_{IJ} &:= \mathbf{I}_{\mathbf{n}_{\text{sd}}} \frac{1}{\mathbf{n}_{\text{fn}}^{e,i}} |\Gamma_{e,j}| \delta_{IJ}. \end{aligned} \quad (39)$$

$$(40)$$

Analogously, the discretisation of the global problem of equation (36) after inserting the expressions of equation (37), leads to a system of equations

$$\begin{bmatrix} \hat{\mathbf{K}}_{\hat{\mathbf{u}}\hat{\mathbf{u}}} & \hat{\mathbf{K}}_{\hat{\mathbf{u}}\hat{\boldsymbol{\rho}}} \\ \hat{\mathbf{K}}_{\hat{\mathbf{u}}\hat{\boldsymbol{\rho}}}^T & \mathbf{0}_{\mathbf{n}_{\text{el}}} \end{bmatrix} \begin{Bmatrix} \hat{\mathbf{u}} \\ \hat{\boldsymbol{\rho}} \end{Bmatrix} = \begin{Bmatrix} \hat{\mathbf{f}}_{\hat{\mathbf{u}}} \\ \hat{\mathbf{f}}_{\hat{\boldsymbol{\rho}}} \end{Bmatrix}, \quad (41)$$

where the global matrix and right hand side are obtained by assembling the elemental contributions given by

$$(\widehat{\mathbf{K}}_{\hat{u}\hat{u}})_{i,j}^e := |\Gamma_{e,i}| \left[\tau_i \tau_j \mathbf{P}_{e,i} (\mathbf{M}_e^{-1} \mathbf{R}_j) - \nu |\Omega_e|^{-1} |\Gamma_{e,j}| (\mathbf{n}_i \cdot \mathbf{n}_j) \mathbf{I}_{\text{nsd}} - \tau_i \delta_{ij} \mathbf{I}_{\text{nsd}} \right], \quad (42a)$$

$$(\widehat{\mathbf{K}}_{\hat{u}\rho})_i^e := |\Gamma_{e,i}| \mathbf{n}_i, \quad (42b)$$

$$(\hat{\mathbf{f}}_{\hat{u}})_i^e := |\Gamma_{e,i}| \left(\nu |\Omega_e|^{-1} \mathbf{n}_i \cdot \mathbf{Z}_e - \tau_i \mathbf{P}_{e,i} (\mathbf{M}_e^{-1} \mathbf{B}_e) - \mathbf{t}_i \chi_{\mathcal{N}_e}(i) \right), \quad (42c)$$

$$(\hat{\mathbf{f}}_{\rho})^e := - \sum_{j \in \mathcal{D}_e} |\Gamma_{e,j}| \mathbf{u}_{D,j} \cdot \mathbf{n}_j, \quad (42d)$$

for $i, j \in \mathcal{B}_e$. The matrix $\mathbf{P}_{e,i}$, introduced to account for the projection of the solution on a space of constant functions on the face $\Gamma_{e,i}$, is defined as

$$\mathbf{P}_{e,i} = \begin{bmatrix} \mathbf{p}_{e,i}^T & \mathbf{0}_{1 \times 3} \\ \mathbf{0}_{1 \times 3} & \mathbf{p}_{e,i}^T \end{bmatrix} \quad (43)$$

and

$$\mathbf{P}_{e,i} = \begin{bmatrix} \mathbf{p}_{e,i}^T & \mathbf{0}_{1 \times 4} & \mathbf{0}_{1 \times 4} \\ \mathbf{0}_{1 \times 4} & \mathbf{p}_{e,i}^T & \mathbf{0}_{1 \times 4} \\ \mathbf{0}_{1 \times 4} & \mathbf{0}_{1 \times 4} & \mathbf{p}_{e,i}^T \end{bmatrix} \quad (44)$$

in two and three dimensions respectively. The vector $\mathbf{p}_{e,i}$ was introduced in equation (20).

4. Mesh adaptivity

As mentioned in section 2.3, the proposed FCFV can be seen as a particular case of the hybridised DG method with reduced stabilisation [24] and therefore provides second-order convergence for the solution.

As mentioned in remark 2, the two key aspects to guarantee second-order convergence are the projection operator used to define the numerical flux and the richer space of approximation used for the primal variable. Without

the projection the method is only first-order accurate. This small difference in the formulation is exploited here to devise an error indicator. Noting u the solution of the proposed FCFV methodology and \tilde{u} the solution of the method where the projection is not performed, the following error indicator is proposed for the Poisson problem

$$E_e = \left[\frac{1}{|\Omega_e|} \int_{\Omega_e} (\tilde{u} - u)^2 d\Omega \right]^{1/2}, \quad (45)$$

with a similar definition for the Stokes problem.

To compute the desired cell size, the error indicator of equation (45) is combined with the a priori local error estimate for elliptic problems [10] given by

$$\varepsilon_e = \|u - u_h\|_{\mathcal{L}_2(\Omega_e)} \leq Ch_e^{1+n_{sd}/2}, \quad (46)$$

for a constant degree of approximation, where h_e is the characteristic cell size and C is a constant independent on the mesh size. By using Richardson extrapolation, the following desired cell size is computed, for a desired error ε ,

$$h_e^* = h_e \left(\frac{\varepsilon}{E_e} \right)^{2+n_{sd}/2}. \quad (47)$$

It is worth noting that the difference between u and \tilde{u} is only due to the use of the projection of the solution over a space of constant functions. Therefore, the majority of the calculations required to assemble the global system of equations can be re-used, substantially reducing the computational effort required to compute the error indicator of equation (45). In fact, as detailed in remark 1, the only difference between both formulations is in the matrix \mathbf{m}_e in equation (25) and \mathbf{M}_e in equation (42) for the Poisson and Stokes problems respectively.

5. Numerical studies

This section presents a series of numerical experiments designed to test the optimal convergence properties of the proposed technique and to compare its performance with the recently proposed first-order FCFV [28]. Numerical experiments are also presented to illustrate the accuracy of the method in terms of the stabilisation parameter and the distortion and the stretching of the meshes. In all the test cases where the analytical solution is known, the relative error in the $\mathcal{L}_2(\Omega)$ norm is used to measure the accuracy of the solution, namely

$$\|E\|_{\mathcal{L}_2(\Omega)} = \frac{\|u - u^{\text{ex}}\|_{\mathcal{L}_2(\Omega)}}{\|u^{\text{ex}}\|_{\mathcal{L}_2(\Omega)}} \quad (48)$$

where u^{ex} denotes the analytical solution.

5.1. Optimal convergence of the second-order FCFV scheme for Poisson equation

A mesh convergence study is performed for the Poisson problem using a series of successively refined triangular meshes. Figure 1 shows the first three levels of mesh refinement. Further levels of mesh refinement are introduced in a similar fashion by subdividing a Cartesian grid. Similarly, for the three dimensional numerical studies performed, the tetrahedral mesh is obtained by subdividing a regular grid of hexahedral elements.

The boundary conditions and source term are selected such that the analytical solution of the problem is known and given by

$$u^{\text{ex}}(\mathbf{x}) = \exp(\alpha \sin(ax_1 + cx_2) + \beta \cos(bx_1 + dx_2)), \quad (49)$$

with $\alpha = 0.1$, $\beta = 0.3$, $a = 5.1$, $b = 4.3$, $c = -6.2$ and $d = 3.4$.

Figure 2 shows the relative $\mathcal{L}_2(\Omega)$ norm of the error of the solution and its gradient as a function of the characteristic mesh size h . The results clearly

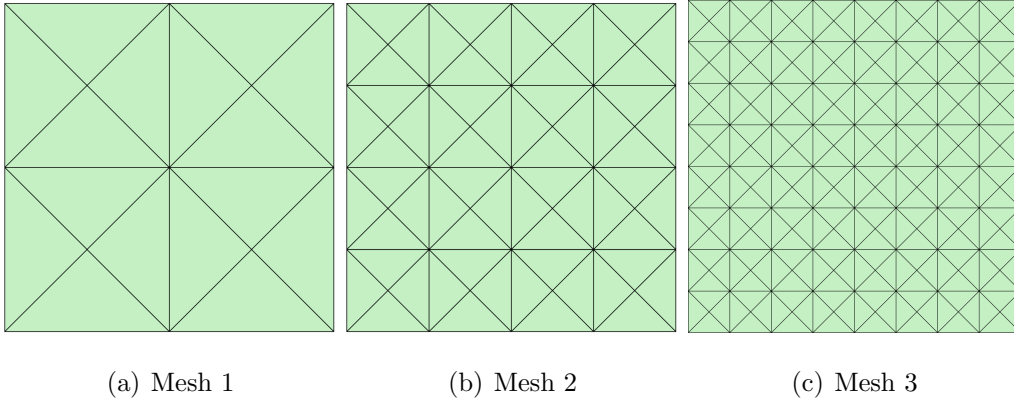


Figure 1: First three meshes used to perform the mesh convergence studies in two dimensions.

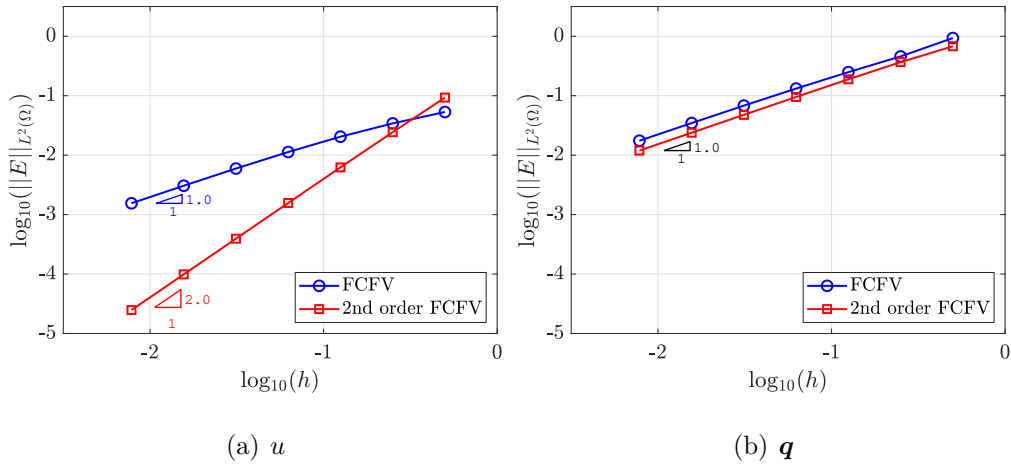


Figure 2: Mesh convergence of the error of the solution and its gradient in the $\mathcal{L}_2(\Omega)$ norm for two dimensional Poisson problem.

show the optimal second-order convergence of the error of the solution and the first-order convergence of the error of the solution gradient. The results of the original FCFV are also included, clearly showing the gain in accuracy achieved for the solution u for a given spatial discretisation. The gradient of the solution is only marginally more accurate as the approximation space for this variable is not changed with respect to the original FCFV.

The results of the analogous study in three dimensions are shown in Fig-

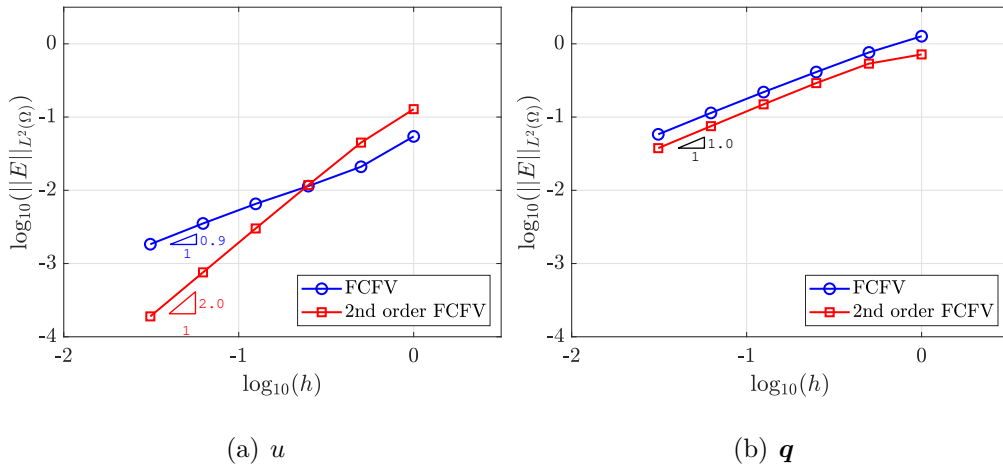


Figure 3: Mesh convergence of the error of the solution and its gradient in the $\mathcal{L}_2(\Omega)$ norm for three dimensional Poisson problem.

ure 3, demonstrating the optimal convergence of the error for both the solution and its gradient as well as the increased accuracy with respect to the first-order FCFV. In this case uniform tetrahedral meshes are used and the boundary conditions and source term are selected so that the analytical solution is known and given by

$$u^{\text{ex}}(\mathbf{x}) = \exp(\alpha \sin(ax_1 + cx_2 + ex_3) + \beta \cos(bx_1 + dx_2 + fx_3)), \quad (50)$$

with $\alpha = 0.1$, $\beta = 0.3$, $a = 5.1$, $b = 4.3$, $c = -6.2$, $d = 3.4$, $e = 1.8$ and $f = 1.7$.

5.2. Optimal convergence of the second-order FCFV scheme for Stokes equation

A mesh convergence is next performed for the Stokes problem in two and three dimensions. For the two dimensional problem the viscosity parameter is set to $\nu = 1$ and the source term and boundary conditions are selected

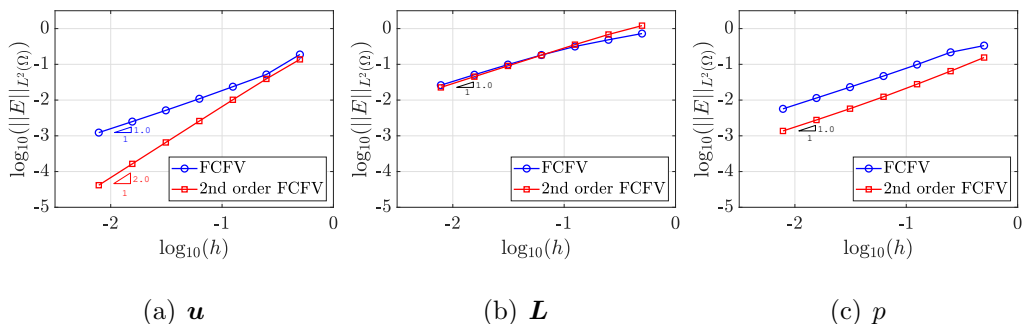


Figure 4: Mesh convergence of the error of the velocity, its gradient and the pressure in the $\mathcal{L}_2(\Omega)$ norm for two dimensional Stokes problem.

such that the analytical solution is

$$\begin{cases} u_1^{\text{ex}}(\mathbf{x}) = x_1^2(1 - x_1)^2(2x_2 - 6x_2^2 + 4x_2^3), \\ u_2^{\text{ex}}(\mathbf{x}) = -x_2^2(1 - x_2)^2(2x_1 - 6x_1^2 + 4x_1^3), \\ p^{\text{ex}}(\mathbf{x}) = x_1(1 - x_1). \end{cases} \quad (51)$$

For the three dimensional problem the viscosity parameter is also set to $\nu = 1$ and the source term and boundary conditions are selected such that the analytical solution is

$$\begin{cases} u_1^{\text{ex}}(\mathbf{x}) = 1/2 + (x_3 - x_2) \sin(x_1 - 1/2), \\ u_2^{\text{ex}}(\mathbf{x}) = 1 - x_2(x_3 - x_2/2) \cos(x_1 - 1/2) - x_2(x_1 - x_2/2) \cos(x_3 - 1/2), \\ u_3^{\text{ex}}(\mathbf{x}) = 1/2 + (x_1 - x_2) \sin(x_3 - 1/2), \\ p^{\text{ex}}(\mathbf{x}) = x_1(1 - x_1) + x_2(1 - x_2) + x_3(1 - x_3). \end{cases} \quad (52)$$

Figures 4 and 5 show relative $\mathcal{L}_2(\Omega)$ norm of the error of the velocity, its gradient and the pressure as a function of the characteristic mesh size h .

The error of the velocity converges with second-order accuracy whereas first-order convergence is observed for its gradient, with an important gain on accuracy in the pressure. For the three dimensional test case, the optimal convergence is again observed for all the variables.

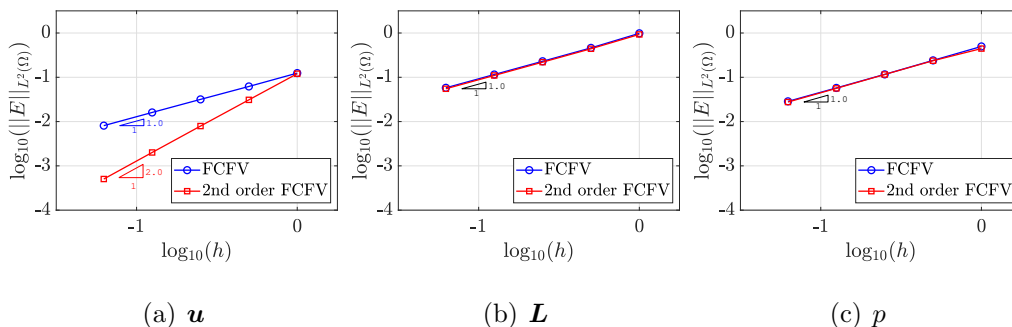


Figure 5: Mesh convergence of the error of the velocity, its gradient and the pressure in the $\mathcal{L}_2(\Omega)$ norm for three dimensional Stokes problem.

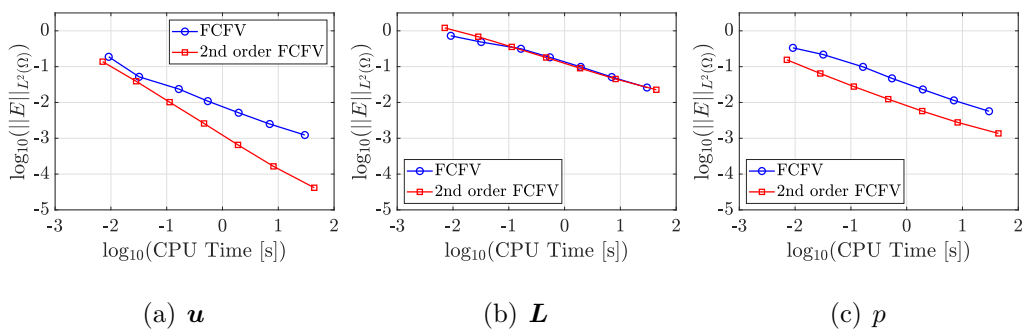


Figure 6: Error of the velocity, its gradient and the pressure in $\mathcal{L}_2(\Omega)$ norm as a function of the CPU time for two dimensional Stokes problem.

5.3. Computational cost

The convergence studies performed in the previous section show an important gain in accuracy of the proposed second-order FCFV method when compared to the original FCFV in the same mesh. In this section both methods are compared in terms of the computational time by using the same meshes and the same problem described in sections 5.1 and 5.2.

Figure 6 shows relative $\mathcal{L}_2(\Omega)$ norm of the error of the velocity, its gradient and the pressure as a function of the CPU time for the two dimensional Stokes problem. The results show that the proposed second-order FCFV is able to produce more accurate results for the velocity and the pressure using the

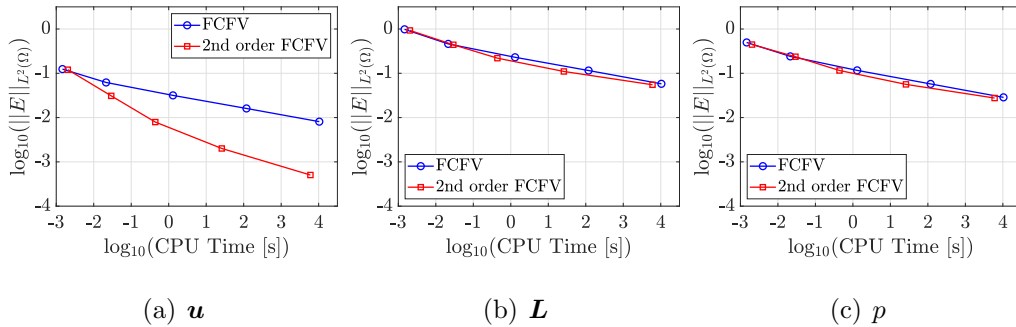


Figure 7: Error of the velocity, its gradient and the pressure in $\mathcal{L}_2(\Omega)$ norm as a function of the CPU time for three dimensional Stokes problem.

same CPU time when compared to the first-order FCFV, whereas similar results are obtained for the velocity gradient. In three dimensions similar conclusions are obtained, as shown in Figure 7. The results show that the proposed second-order FCFV provides the same accuracy as the original first-order FCFV with orders of magnitude less CPU time when the velocity is of interest. For instance, an error in the velocity field of the order of 1% is obtained in less than 1 second with the second-order FCFV whereas the first-order FCFV requires 2.7 hours.

The results for the Poisson problem, not displayed here for brevity, show the same advantages for the proposed second-order FCFV.

5.4. Influence of the stabilisation parameter

The next study considers the influence of the stabilisation parameter τ in the accuracy of the proposed second-order FCFV method using the same meshes and the same problem described in sections 5.1 and 5.2.

Figure 8 shows the relative error, measured in the $\mathcal{L}_2(\Omega)$ norm, as a function of the stabilisation parameter for the two and three dimensional Poisson problem and for two levels of mesh refinement. The results show that a maximum accuracy in the solution is achieved for a value of the stabilisation

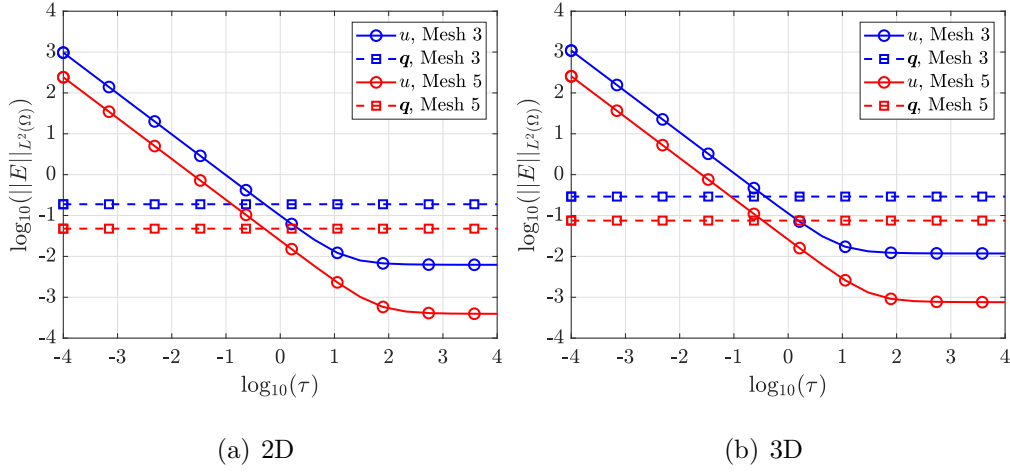


Figure 8: Error of the solution and its gradient in $\mathcal{L}_2(\Omega)$ norm as a function of stabilisation parameter τ for Poisson problem.

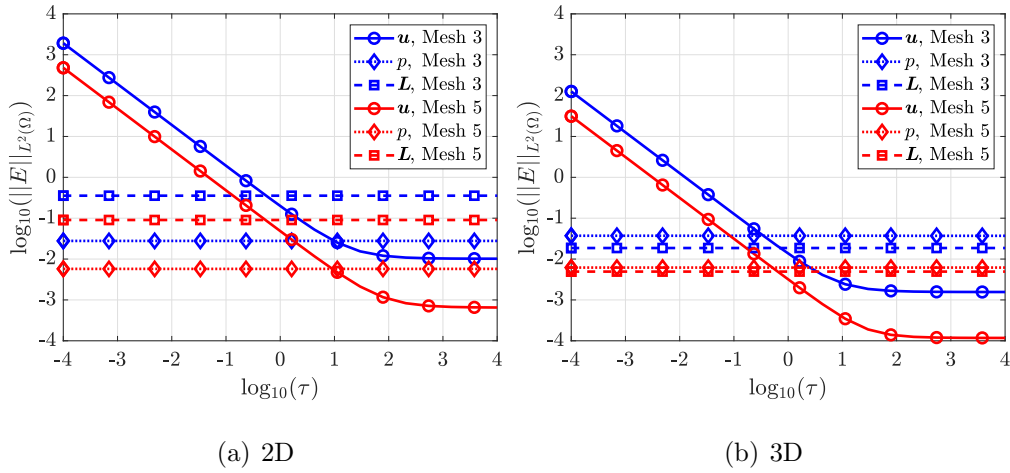


Figure 9: Error of the velocity, its gradient and the pressure in $\mathcal{L}_2(\Omega)$ norm as a function of stabilisation parameter τ for Stokes problem.

parameter of 10^2 or larger, whereas the error of the solution gradient seems insensitive to the choice of this parameter. The behaviour is almost identical in both two and three dimensions.

For the Stokes problem, similar conclusions are obtained, as illustrated in Figure 9. In this case, the velocity gradient and the pressure are insensitive

to the stabilisation parameter τ , whereas the velocity requires a value of 10^2 or larger to provide the maximum accuracy.

It is worth emphasising that the value required to achieve the maximum accuracy of the solution is the same for two and three dimensional problems and for Poisson and Stokes problems. In addition, compared to the results presented in [28] for the first-order FCFV, the proposed second-order FCFV is less sensitive to a particular choice of the stabilisation parameter.

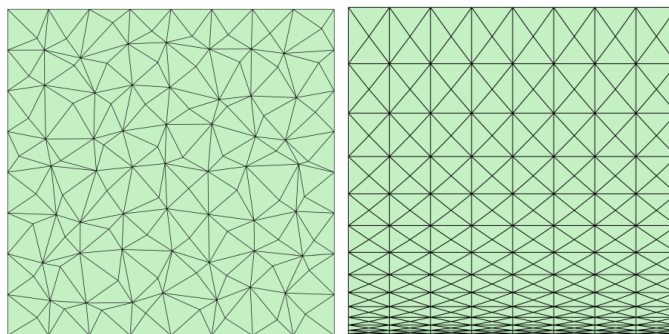
It is also worth mentioning that further numerical examples, not reported here for brevity, confirm that the conclusions extracted from these numerical experiments do not depend upon the spatial discretisation or the problem. Identical behaviour has been observed for both Poisson and Stokes problems, in two and three dimensions and for different levels of mesh refinement.

5.5. Influence of the cell distortion and stretching

The last study considers the solution of Poisson and Stokes problems in meshes involving distorted and stretched cells. To illustrate the type of cells tested, Figure 10 shows the mesh corresponding to the third level of refinement where the cells have been randomly distorted, as explained in [28] and with stretched cells with a stretching factor of 100.

Figure 11 shows a mesh convergence study for the Poisson problem in two and three dimensional meshes that have been distorted by randomly moving the interior nodes (i.e. the nodes not on the boundary of the domain) as described in [28]. The results are almost identical to the ones obtained for regular meshes and displayed in Figures 2 and 3, showing that the proposed method is insensitive to mesh distortion.

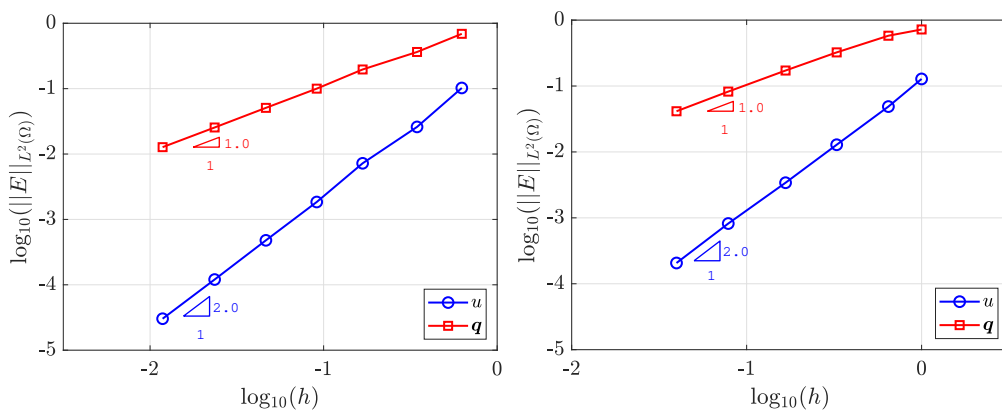
The same conclusions are also obtained for the Stokes problem in two and three dimensions as shown in Figure 12.



(a) Distorted cells

(b) Stretched cells

Figure 10: Mesh with (a) distorted and (b) stretched cells to test the sensitivity of the FCFV to mesh quality.



(a) 2D

(b) 3D

Figure 11: Mesh convergence of the error of the solution and its gradient in $\mathcal{L}_2(\Omega)$ norm for 2D and 3D Poisson problem with irregular mesh.

Next, the influence of the cell stretching is considered. Two cases involving a maximum stretching factor, s , of 10 and 1,000 are considered, where this factor is measured in each cell as the ratio between the longest and the shortest edges. Figure 13 shows the relative $\mathcal{L}_2(\Omega)$ norm of the error of the solution and its gradient as a function of the characteristic mesh size for the Poisson problem solved in stretched meshes in two and three dimensions.

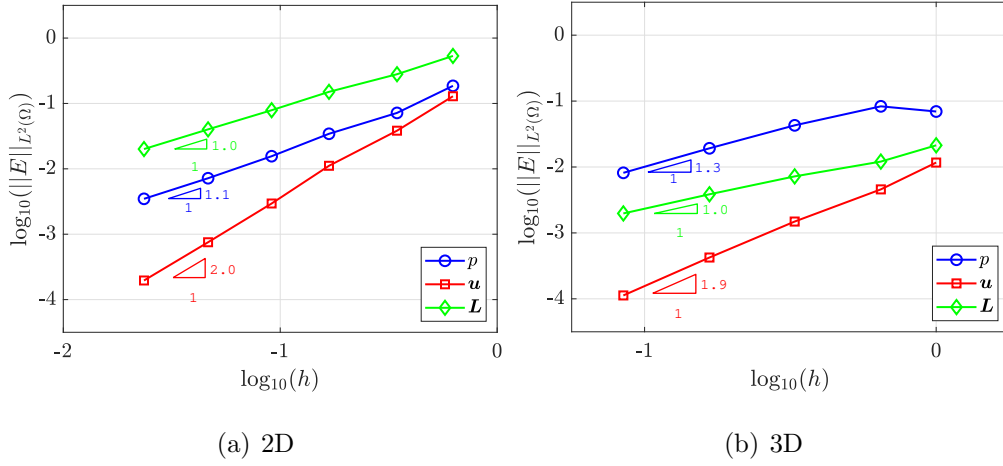


Figure 12: Mesh convergence of the error of the velocity, its gradient and the pressure in $\mathcal{L}_2(\Omega)$ norm for 2D and 3D Stokes problem with irregular mesh.

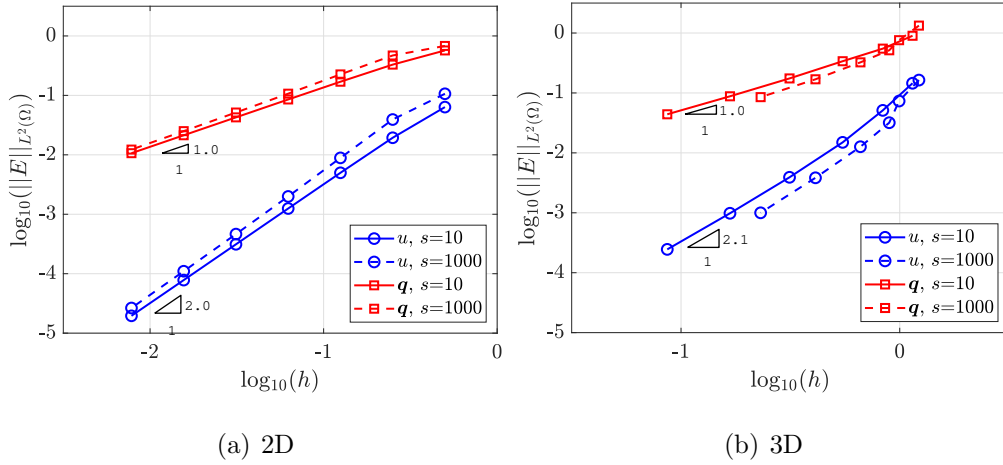


Figure 13: Mesh convergence of the error of the solution and its gradient in $\mathcal{L}_2(\Omega)$ norm for 2D and 3D Poisson problem with stretched meshes with stretching factor $s = 10$ and $s = 1,000$.

Almost identical results are observed for both stretching factors. In the two dimensional problem a marginal lower error is observed for the mesh with stretching factor $s = 10$ whereas for the three dimensional problem the mesh with stretching factor $s = 1,000$ produces a slightly lower error.

The results for the Stokes problem in two and three dimensions are dis-

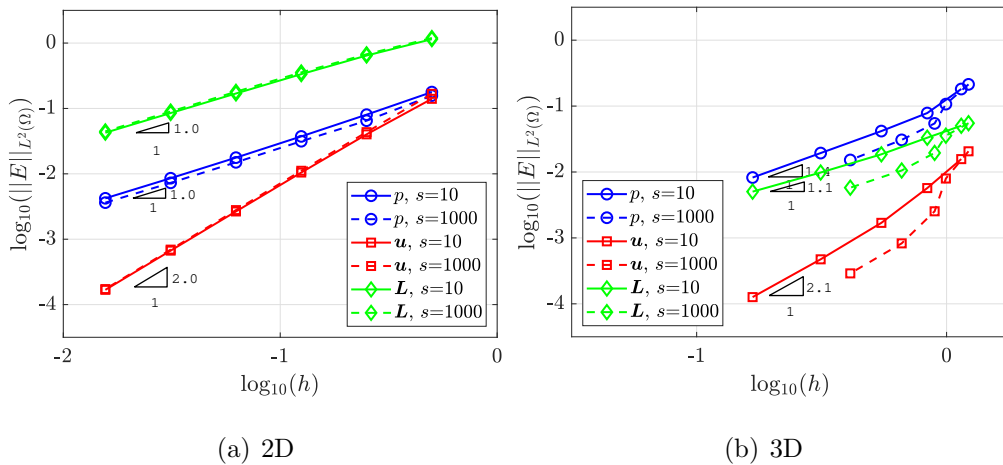


Figure 14: Mesh convergence of the error of the velocity, its gradient and the pressure in $\mathcal{L}_2(\Omega)$ norm for 2D and 3D Stokes problem with stretched meshes with stretching factor $s = 10$ and $s = 1,000$.

played in Figure 14, confirming the conclusions observed for the Poisson problem.

It is worth noting that contrary to other FV methods, the proposed second-order FCFV method not only shows an accuracy that is insensitive to mesh distortion and stretching but also preserves the optimal rate of convergence in all the variables, i.e. the solution and its gradient for the Poisson problem and the velocity, its gradient and the pressure for the Stokes problem.

6. Numerical examples

6.1. Irrotational flow past a full aircraft

To show the ability of the proposed method to efficiently solve large scale problems involving complex geometries, the irrotational flow around a full aircraft is considered. A tetrahedral mesh with 5,125,998 cells is considered, leading to a global system of 11,283,113 equations to find the solution on

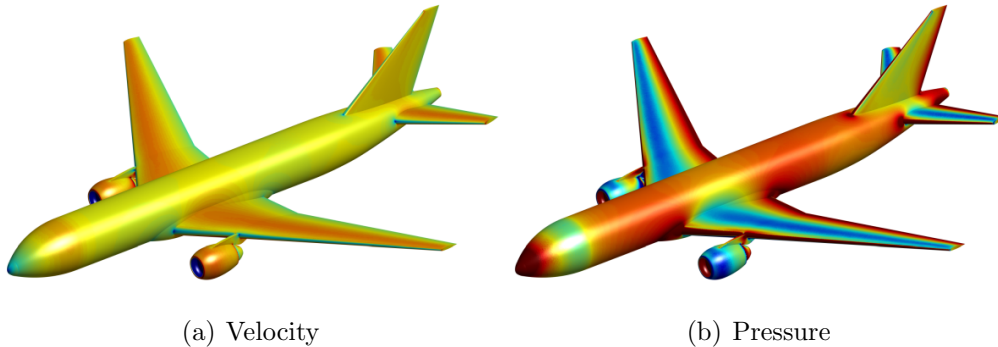


Figure 15: Magnitude of the velocity and pressure distribution for the irrotational flow around a full aircraft configuration.

the cell faces. The magnitude of the velocity, computed from the gradient of the solution, and the pressure, computed from the Bernoulli equation are displayed in Figure 15.

The solution using the proposed second-order FCFV took 5.1 minutes for the computation of all the elemental matrices and the assembly and 6.4 minutes to solve the global system of equations using a direct method. The developed code is written in Matlab and the computation was performed in an Intel® Xeon® CPU @ 3.70GHz and 32GB main memory available.

It is worth noting that the time required to assemble the system of equations is slightly higher than the time reported in [28] for the first-order FCFV, namely 3.7 minutes. This difference is due to the extra operations required by the second-order method for the computation and assembly of the global matrix as a result of the larger approximation space used for the primal variable. The time required by the proposed second-order FCFV to solve the system is almost identical to the time employed by the first-order method, 5.7 minutes, due to the global matrix having the exact same size and structure, with the same number of non-zero elements.

Finally, it is worth noting that, as shown in section 5.3, the extra cost

induced by the second-order FCFV for a given spatial discretisation leads, in all the examples studied, to a substantial gain in accuracy. In general, for a given error, the proposed FCFV is more efficient due to the second-order accuracy obtained for the primal variable.

6.2. Stokes flow past a sphere

The next example considers the Stokes flow around a sphere. This classical three dimensional example is used to compare the accuracy and performance of the proposed second-order FCFV against the original first-order FCFV method for a problem involving large three dimensional meshes. The domain of interest is $\Omega = ([-7, 15] \times [-5, 5] \times [-5, 5]) \setminus \mathcal{B}_{1,0}$, where $\mathcal{B}_{1,0}$ is the unit ball with centre at the origin. Homogeneous Neumann boundary conditions are imposed on the outlet part of the boundary, corresponding to $x = 15$, whereas Dirichlet boundary conditions, corresponding to the exact solution, are imposed on the rest of the boundary.

Six unstructured tetrahedral meshes are considered with 3,107, 10,680, 43,682, 204,099, 686,853 and 2,516,099 cells respectively. The size of the global system of equations to be solved to obtain the velocity on the cell faces is 20,711, 72,249, 299,276, 1,409,916, 4,765,776 and 17,513,075 respectively.

Figure 16(a) shows the convergence of the error for the velocity, pressure and gradient of the velocity as the mesh is refined. The results are compared to the original first-order FCFV and clearly show the advantage of the proposed method by providing second-order convergence on the velocity. In this example the accuracy for the other variables is almost identical, with a marginal gain observed in the computation of the pressure in the finest meshes. Figure 16(b) shows the convergence of the drag as the mesh is refined. The advantages of the proposed second-order FCFV are observed as the convergence to the exact value is faster than with the original first-order

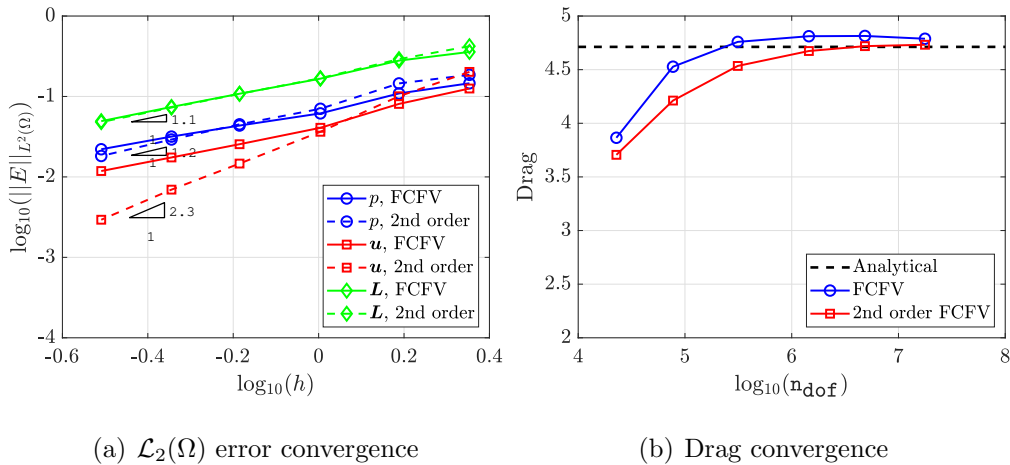


Figure 16: Comparison between first and second-order FCFV for the Stokes flow past a sphere. (a) Convergence of the error of velocity, pressure and gradient of the velocity in the $L_2(\Omega)$ norm and (b) convergence of the drag.

method. It is worth mentioning that, differently from the simulations in [28], the results in figure 16 are obtained imposing a homogeneous Neumann condition on the portion of the boundary representing the physical outflow, both for the first-order and second-order FCFV. This choice stems from the engineering practice of imposing a free traction on the outflow, instead of a given velocity profile.

6.3. Mesh adaptivity for the Poisson problem

This section presents a numerical example to illustrate the strategy described in section 4 to perform an automatic mesh adaptive process by combining the results of the first-order and second-order FCFV methods. A two dimensional Poisson problem with known analytical solution is considered in $\Omega = [0, 1]^2$. The source term and Dirichlet boundary conditions are selected so that the analytical solution is given by

$$u^{\text{ex}}(x_1, x_2) = \exp\left(-100 \left[(x_1 - 0.7)^2 + (x_2 - 0.7)^2\right]\right) \quad (53)$$

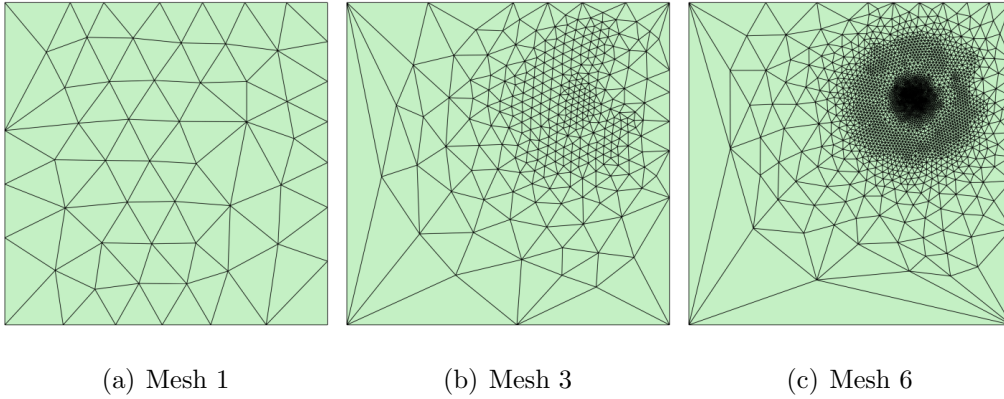


Figure 17: Three meshes used in the automatic mesh adaptive process for the Poisson problem.

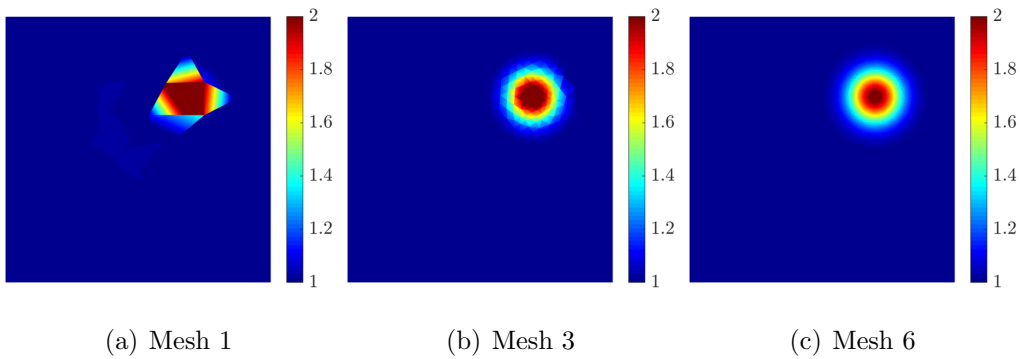


Figure 18: Three FCFV approximations corresponding to the meshes of Figure 17.

and the desired accuracy is $\varepsilon = 10^{-2}$.

The process starts with the coarse mesh represented in Figure 17(a). The approximation with the proposed FCFV on the coarsest mesh is depicted in Figure 18(a). By comparing the approximation of the second-order FCFV with the approximation of the first-order FCFV method (i.e. without the projection operator), a desired cell size is computed, using equation (47), and a new mesh is generated. The mesh and the second-order FCFV approximation after two iterations of the mesh adaptive process are displayed in Figures 17(b) and 18(b) respectively. It can be clearly observed how the

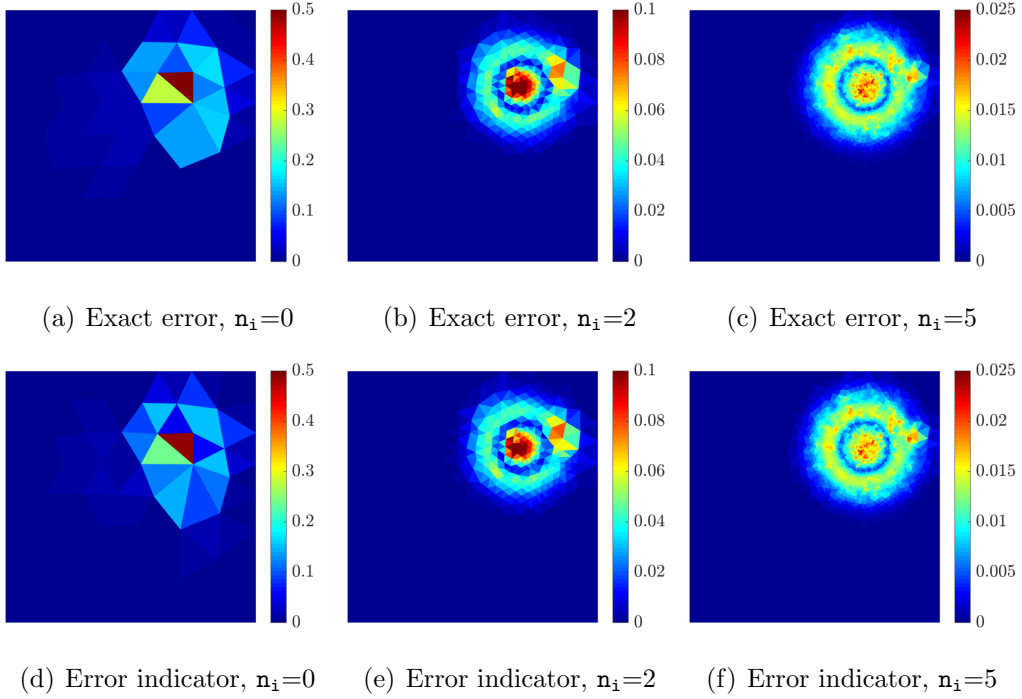


Figure 19: Exact error and indicator map in the $\mathcal{L}_2(\Omega_e)$ norm for the three stages of the adaptive process corresponding to the meshes and approximations shown in Figures 17 and 18.

mesh is coarsened in the regions where the approximation is almost constant, whereas the mesh density is increased in the regions where the approximation changes rapidly. The adaptive process finishes in five iterations, when the desired error is achieved. The final mesh and FCFV approximation are represented in Figures 17(c) and 18(c) respectively.

As described in section 4, the adaptive process is driven by an error indicator that results from computing the relative difference in each cell, measured in the $\mathcal{L}_2(\Omega_e)$ norm. To illustrate the efficiency of the proposed error indicator, Figure 19 shows both the error indicator and the exact error for the three iterations, n_i , of the adaptive process corresponding to the meshes and approximations shown in Figures 17 and 18.

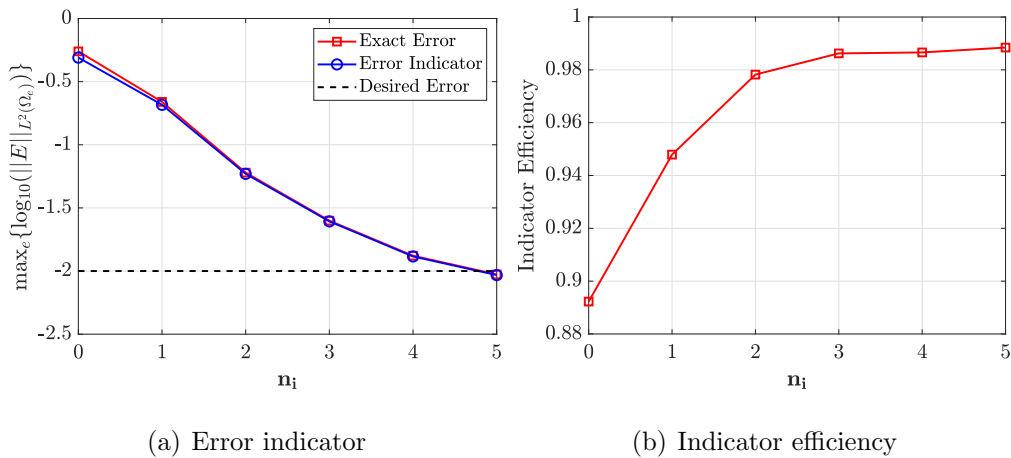


Figure 20: (a) Maximum value of the indicator and the exact error over all the cells and (b) indicator efficiency.

To further illustrate the performance of the error indicator and the automatic adaptive process, Figure 20(a) shows the maximum value of the indicator and the exact error over all the cells as a function of the number of iterations of the mesh adaptive process. The efficiency of the error indicator, defined as the ratio between the exact error and the indicator is also displayed in Figure 20(b), clearly illustrating the suitability of the proposed technique to drive an automatic mesh adaptive process.

6.4. Mesh adaptivity for the Stokes problem

The last example involves the solution of the Stokes equations in three dimensions for the complex geometry, taken from [34], depicted in Figure 21. The corrugated channel has a height of $0.5\mu\text{m}$ and the curved profile is obtained by repeating the expression

$$y = \begin{cases} \frac{1}{2} (f_w + f_n) + \frac{1}{2} (f_w - f_n) \cos\left(\frac{8\pi(2x-L)}{7L}\right) & \text{if } |x| < \frac{15}{16}L, \\ f_n & \text{if } \frac{15}{16}L \leq |x| \leq L, \end{cases} \quad (54)$$

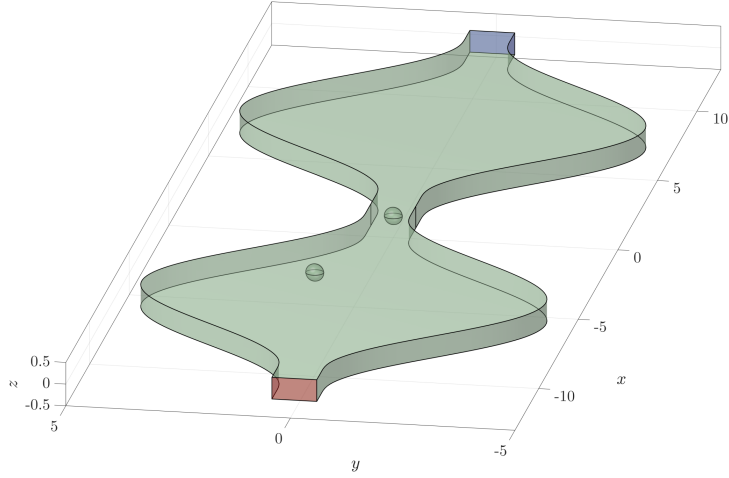


Figure 21: Geometry description for the computation of the Stokes flow in a corrugated channel with two spheres.

where $f_n = 0.5\mu\text{m}$, $f_w = 4.5\mu\text{m}$ and $L = 12.5\mu\text{m}$. Two spheres of radius $0.2\mu\text{m}$ are placed inside the channel. The first sphere, with centre $(0, 0, 0.25)\mu\text{m}$, is placed in the middle of the channel, where the cross section is minimum, and it is expected to produce a major flow disturbance. The second sphere, with centre at $(-3.75, 1, 0.25)\mu\text{m}$, is situated in a region with larger cross section and it is expected to disturb much less the flow. This scenario is utilised to show the ability of the proposed method to drive the adaptivity for a problem involving an incompressible flow in a complex geometry.

A Dirichlet boundary condition, corresponding to a velocity inlet given by $\mathbf{u}_D(x, y, z) = 64(y^2 - 1/4)(z^2 - 1/16)$, is introduced at one end of the channel, at $x = -L$, depicted in red in Figure 21. A homogeneous Neumann boundary condition is imposed at the outlet, at $x = L$, depicted in blue in Figure 21. Homogeneous Dirichlet boundary conditions are imposed on the rest of the boundary, corresponding to material walls.

The initial mesh, shown in Figure 22 (a), has 37,415 tetrahedral cells.

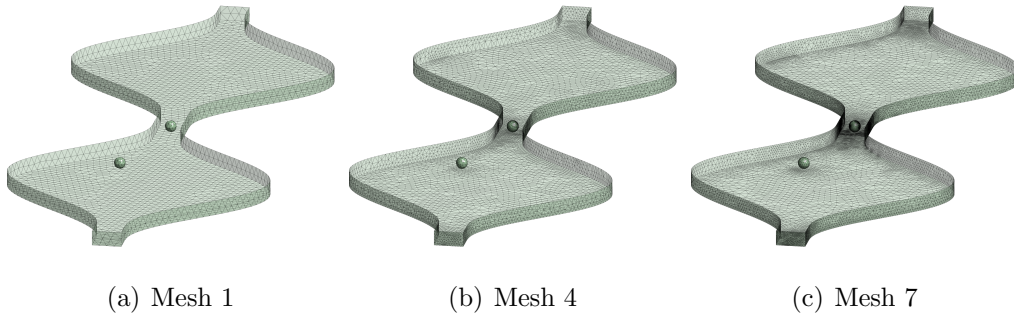


Figure 22: Three of the meshes used for the adaptive computation of the Stokes flow in a corrugated channel with two spheres.

The initial mesh is generated with a required element size of $0.05\mu\text{m}$ on the surfaces defining two spheres, to ensure an appropriate geometric representation. An element size of $0.5\mu\text{m}$ is imposed in the domain, with a smooth transition between these two values.

Next, the automatic adaptive process described in section 4 is applied, with a desired accuracy of $\varepsilon = 5 \times 10^{-2}$. Convergence of the estimated error to the desired tolerance is achieved in this example after seven iterations of the adaptive process. The resulting meshes in the fourth and seven iteration are depicted in Figures 22 (b) and (c) respectively. The fourth mesh has 61,871 cells, with a minimum and maximum element size of $0.010\mu\text{m}$ and $0.594\mu\text{m}$ respectively. The last mesh has 116,913 cells, with a minimum and maximum element size of $0.003\mu\text{m}$ and $0.520\mu\text{m}$ respectively. A detailed view of the three meshes of Figure 22 near the two spheres is shown in Figure 23.

The velocity streamlines and the pressure field obtained using the last mesh are represented in Figure 24. A detailed view of the velocity streamlines and the pressure field near the sphere surfaces is shown in Figure 25. This Figure offers a qualitative comparison of the major disturbance caused by one sphere compared to the other.

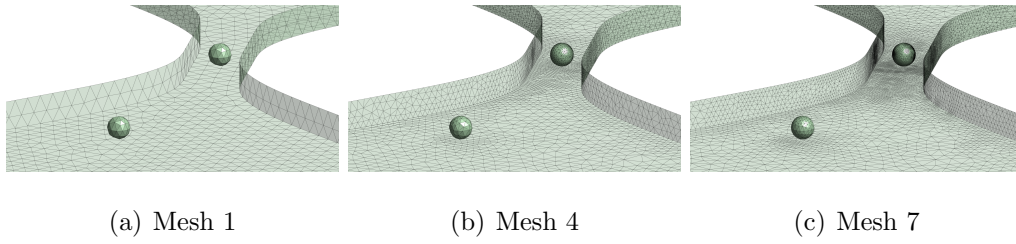


Figure 23: Detailed view of three of the meshes shown in Figure 22.

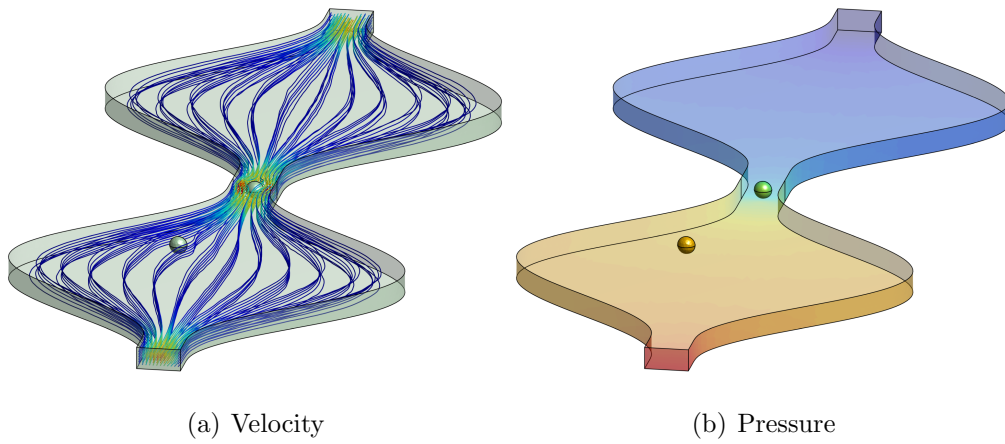


Figure 24: (a) Velocity streamlines and (b) pressure field, obtained in the mesh of Figure 22 (c), at the last iteration of the adaptive computation.

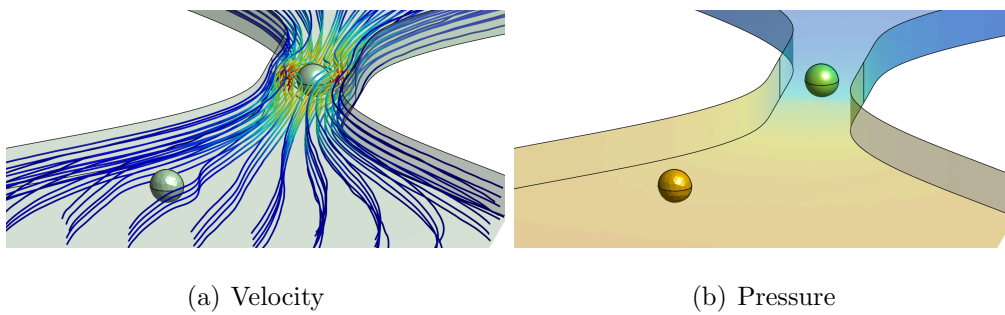


Figure 25: Detailed view of the (a) velocity streamlines and (b) pressure field, obtained in the mesh of Figure 22 (c), at the last iteration of the adaptive computation.

7. Concluding remarks

This paper proposes a second-order FCFV method for the solution of scalar and vector elliptic problems in two and three dimensions. Thus, as in standard finite volumes, piece-wise constant approximations are used on each face and explicit expressions for the matrix coefficients are obtained.

The proposed method preserves the attractive properties of the original first-order FCFV method, namely the first-order convergence of the gradient of the solution, without the need of a reconstruction, and the insensitivity to mesh distortion and stretching. It also satisfies the LBB condition in the context of incompressible flows. Contrary to the original FCFV, the proposed method guarantees second-order convergence of the solution. Numerical experiments show an increased performance when compared to the first-order method in terms of the CPU time required to achieve a desired accuracy as well as a lower sensitivity to the choice of the stabilisation parameter. A combination of first-order and second-order schemes is used to devise an error indicator that can be used to drive a mesh adaptivity process. An extensive set of numerical experiments has been used to demonstrate the optimal approximation properties of the method and more complex problems demonstrate its potential for large scale three dimensional simulations, including a Stokes problem where an automatic mesh adaptive process is employed.

Acknowledgements

This work was partially supported by the European Union's Horizon 2020 research and innovation programme under the Marie Skłodowska-Curie Actions (Grant numbers: 675919 and 764636). The first author gratefully acknowledges the financial support of the Erasmus+ programme. The second, third and last author were also supported by the Spanish Ministry of Econ-

omy and Competitiveness (Grant agreement No. DPI2017-85139-C2-2-R). The second and last authors are grateful for the financial support provided by the Generalitat de Catalunya (Grant agreement No. 2017-SGR-1278).

References

- [1] M. Aguirre, A. J. Gil, J. Bonet, and C. H. Lee. An upwind vertex centred finite volume solver for Lagrangian solid dynamics. *Journal of Computational Physics*, 300:387–422, 2015.
- [2] T. Barth and M. Ohlberger. Finite volume methods: Foundation and analysis. In *Encyclopedia of Computational Mechanics*. John Wiley & Sons, Ltd, 2004.
- [3] J.-C. Chassaing, X. Nogueira, and S. Khelladi. Moving kriging reconstruction for high-order finite volume computation of compressible flows. *Computer Methods in Applied Mechanics and Engineering*, 253:463–478, 2013.
- [4] B. Cockburn, B. Dong, and J. Guzmán. A superconvergent LDG-hybridizable Galerkin method for second-order elliptic problems. *Mathematics of Computation*, 77(264):1887–1916, 2008.
- [5] B. Cockburn and J. Gopalakrishnan. A characterization of hybridized mixed methods for second order elliptic problems. *SIAM Journal on Numerical Analysis*, 42(1):283–301, 2004.
- [6] B. Cockburn and J. Gopalakrishnan. Incompressible finite elements via hybridization. I. The Stokes system in two space dimensions. *SIAM Journal on Numerical Analysis*, 43(4):1627–1650, 2005.

- [7] B. Cockburn and J. Gopalakrishnan. New hybridization techniques. *GAMM-Mitt.*, 28(2):154–182, 2005.
- [8] B. Cockburn, J. Gopalakrishnan, and R. Lazarov. Unified hybridization of discontinuous Galerkin, mixed, and continuous Galerkin methods for second order elliptic problems. *SIAM Journal on Numerical Analysis*, 47(2):1319–1365, 2009.
- [9] B. Cockburn, N. C. Nguyen, and J. Peraire. A comparison of HDG methods for Stokes flow. *Journal of Scientific Computing*, 45(1-3):215–237, 2010.
- [10] P. Díez and A. Huerta. A unified approach to remeshing strategies for finite element h -adaptivity. *Computer Methods in Applied Mechanics and Engineering*, 176(1-4):215–229, 1999.
- [11] B. Diskin and J. L. Thomas. Comparison of node-centered and cell-centered unstructured finite-volume discretizations: inviscid fluxes. *AIAA journal*, 49(4):836–854, 2011.
- [12] B. Diskin, J. L. Thomas, E. J. Nielsen, H. Nishikawa, and J. A. White. Comparison of node-centered and cell-centered unstructured finite-volume discretizations: viscous fluxes. *AIAA journal*, 48(7):1326, 2010.
- [13] J. Donea and A. Huerta. *Finite Element Methods for Flow Problems*. Finite Element Methods for Flow Problems. John Wiley & Sons, 2003.
- [14] J. Droniou. Finite volume schemes for diffusion equations: Introduction to and review of modern methods. *Mathematical Models and Methods in Applied Sciences*, 24(08):1575–1619, 2014.

- [15] R. Eymard, T. Gallouët, and R. Herbin. Finite volume methods. *Handbook of Numerical Analysis*, 7:713 – 1018, 2000. Solution of Equation in \mathbb{R}^n (Part 3), Techniques of Scientific Computing (Part 3).
- [16] M. Giacomini, A. Karkoulas, R. Sevilla, and A. Huerta. A superconvergent HDG method for Stokes flow with strongly enforced symmetry of the stress tensor. *Journal of Scientific Computing*, 77(3):1679–1702, 2018.
- [17] R. J. LeVeque. *Finite volume methods for hyperbolic problems*. Cambridge Texts in Applied Mathematics. Cambridge University Press, Cambridge, 2002.
- [18] A. Montlaur, S. Fernández-Méndez, and A. Huerta. Discontinuous Galerkin methods for the Stokes equations using divergence-free approximations. *International Journal for Numerical Methods in Fluids*, 57(9):1071–1092, 2008.
- [19] K. W. Morton and T. Sonar. Finite volume methods for hyperbolic conservation laws. *Acta Numerica*, 16:155–238, 2007.
- [20] N. Nguyen, J. Peraire, and B. Cockburn. A hybridizable discontinuous Galerkin method for Stokes flow. *Computer Methods in Applied Mechanics and Engineering*, 199(9-12):582–597, 2010.
- [21] N. C. Nguyen, J. Peraire, and B. Cockburn. An implicit high-order hybridizable discontinuous Galerkin method for linear convection-diffusion equations. *Journal of Computational Physics*, 228(9):3232–3254, 2009.
- [22] N. C. Nguyen, J. Peraire, and B. Cockburn. An implicit high-order hybridizable discontinuous Galerkin method for nonlinear convection-

- diffusion equations. *Journal of Computational Physics*, 228(23):8841–8855, 2009.
- [23] N. C. Nguyen, J. Peraire, and B. Cockburn. An implicit high-order hybridizable discontinuous Galerkin method for the incompressible Navier–Stokes equations. *Journal of Computational Physics*, 230(4):1147–1170, 2011.
- [24] I. Oikawa. A hybridized discontinuous Galerkin method with reduced stabilization. *Journal of Scientific Computing*, 65(1):327–340, 2015.
- [25] I. Oikawa. Analysis of a reduced-order HDG method for the Stokes equations. *Journal of Scientific Computing*, 67(2):475–492, 2016.
- [26] W. Qiu and K. Shi. A superconvergent HDG method for the incompressible Navier–Stokes equations on general polyhedral meshes. *IMA Journal of Numerical Analysis*, 36(4):1943–1967, 2016.
- [27] R. Sevilla. HDG-NEFEM for two dimensional linear elasticity. *Computers & Structures*, 220:69–80, 2019.
- [28] R. Sevilla, M. Giacomini, and A. Huerta. A face-centred finite volume method for second-order elliptic problems. *International Journal for Numerical Methods in Engineering*, 115(8):986–1014, 2018.
- [29] R. Sevilla, M. Giacomini, and A. Huerta. A locking-free face-centred finite volume (FCFV) method for linear elastostatics. *Computers & Structures*, 212:43–57, 2019.
- [30] R. Sevilla, M. Giacomini, A. Karkoulas, and A. Huerta. A superconvergent hybridizable discontinuous Galerkin method for linear elasticity.

- International Journal for Numerical Methods in Engineering*, 116(2):91–116, 2018.
- [31] R. Sevilla and A. Huerta. Tutorial on Hybridizable Discontinuous Galerkin (HDG) for second-order elliptic problems. In J. Schröder and P. Wriggers, editors, *Advanced Finite Element Technologies*, volume 566 of *CISM International Centre for Mechanical Sciences*, pages 105–129. Springer International Publishing, 2016.
- [32] R. Sevilla and A. Huerta. HDG-NEFEM with degree adaptivity for Stokes flows. *Journal of Scientific Computing*, 77(3):1953–1980, 2018.
- [33] E. F. Toro. *Riemann solvers and numerical methods for fluid dynamics*. Springer-Verlag, Berlin, third edition, 2009. A practical introduction.
- [34] X. Yang, C. Liu, Y. Li, F. Marchesoni, P. Hänggi, and H. Zhang. Hydrodynamic and entropic effects on colloidal diffusion in corrugated channels. *Proceedings of the National Academy of Sciences*, 114(36):9564–9569, 2017.